SEMARAK ILMU PUBLISHING

Journal of Advanced Research in Fluid Mechanics and Thermal Sciences

Journal homepage:
https://semarakilmu.com.my/journals/index.php/fluid_mechanics_thermal_sciences/index
ISSN: 2289-7879

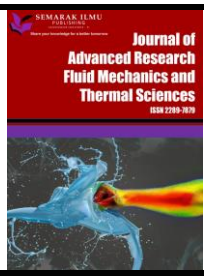

Overlapping Multi-Domain Paired Quasilinearization Method for the Solution of the MHD Williamson-Nanofluid Flow Over an Exponentially Stretching Surface

Mpho Mendy Nefale[1,*], Mekonnen Shiferaw Ayano[2], Olumuyiwa Otegbeye[1], Shina Daniel Oloniiju[3]

[1] School of Computer Science and Applied Mathematics, University of the Witwatersrand, Johannesburg, South Africa
[2] Department of Mathematics, University of Eswatini, Kwaluseni, Eswatini
[3] Department of Mathematics, Rhodes University, Makhanda, PO Box 94, Grahamstown 6140, South Africa

ARTICLE INFO

Article history:
Received 17 August 2024
Received in revised form 6 December 2024
Accepted 16 December 2024
Available online 10 January 2025

Keywords:
Williamson model; nanofluid; magnetohydrodynamics; spectral methods

ABSTRACT

This study examines a non-Newtonian fluid model representing shear-thinning behaviour with applications in both biological and industrial fields. While prior research has investigated the fluid's dynamics in various contexts, the combined effects of the Williamson fluid model and additional parameters remain underexplored. This work focuses on the analysis of magnetohydrodynamic Williamson-nanofluid flow over an exponentially stretched surface. To solve the transformed model equations, an advanced numerical approach, the overlapping multi-domain paired quasilinearization method (OMD-PQLM), is employed. This method enhances the traditional paired quasilinearization method (PQLM) by subdividing the integration interval with overlapping techniques, enabling efficient and accurate solutions to the nonlinear ODEs. Key parameters studied include the Hall parameter, chemical reaction parameter, thermophoresis particle parameter, Brownian motion parameter, and magnetic parameter. Notably, the Williamson parameter significantly affects velocity profiles, temperature distribution, and concentration, with its shear-thinning properties altering flow characteristics and leading to higher temperature and concentration distributions. The OMD-PQLM demonstrated superior accuracy compared to the standard PQLM. This comprehensive analysis provides valuable insights into the OMD-PQLM's effectiveness and the behaviour of Williamson-nanofluid systems under various conditions, contributing to advancements in nanofluid applications, air conditioning, cooling processes, and thermal energy storage.

1. Introduction

Williamson [1] developed the Williamson fluid model, a non-Newtonian fluid exhibiting shear-thinning properties. The Williamson fluid model is applied in various biological and industrial settings, particularly in the production of emulsion sheets, such as photographic films, as well as in the study of plasma and blood flow referenced in previous studies [2-7]. Nadeem and Akbar [8] investigated

* *Corresponding author.*
E-mail address: nefalempho97@gmail.com

https://doi.org/10.37934/arfmts.126.1.1738

the peristaltic transport of Williamson fluid in an endoscope using the homotopy analysis method based on Liao [9]. Their findings revealed that an increase in the non-Newtonian Williamson parameter leads to a decrease in flow velocity. Similarly, Nadeem and Hussain [10] examined the impact of nanoparticles on the boundary layer flow of Williamson fluid over a dilating surface using the homotopy analysis method. Their study demonstrated that both the width of the boundary layer and the velocity decrease as the Williamson parameter is increased. Gorla and Gireesha [11] numerically investigated heat transfer characteristics on a linearly stretching surface in Williamson nanofluids. The analysis applied the Runge-Kutta–Felhberg fourth-fifth order method (RKF45) along with the shooting approach [12]. The findings revealed that higher values of the Williamson parameter corresponded to an increased thermal boundary thickness.

Choi [13] proposed the addition of nanofluid to enhance the thermal properties of the fluid, which has attracted the interest of many researchers. The concept proposed by Choi [13] has been used to improve the heat transfer rate in liquids. Mkhatshwa *et al.,* [14] studied the MHD mixed convection nanofluid flow around a vertical slender cylinder and reported that augmentation to the nanoparticle volume fraction also enhances skin friction. They used the overlapping multi-domain bivariate spectral quasilinearization method (OMD-BSQLM) introduced by Mkhatshwa *et al.,* [15], which proved to be accurate and enabled the authors to investigate the impact of various parameters. Shehzad *et al.,* [16] investigated the stagnation point flow of nanofluid over a heated shrinking sheet using the finite difference technique in conjunction with the RKF45 method with a shooting technique, and it was reported that mass transfer improves with the augmentation of the thermophoresis parameter.

In addition, Galal *et al.,* [17] studied the effectiveness and accuracy of a single-trained artificial neural network for heat and mass transfer in magnetized hybrid nanofluid flow within a rotating permeable system. The heat and mass transfer rate for three-dimensional magnetohydrodynamic nanoliquid movement with thermal radiation and chemical reaction over a dual stretchable surface in the presence of an inclined magnetic field and viscous dissipation was examined by Galal *et al.,* [18]. One of the results reported showed that a change in the angle of inclination performance was noted at 8% for nanofluid and 33% for hybrid nanofluid. The nanofluid flow confined between two parallel sheets, focusing on thermophoresis and Brownian motion, was examined by Zar *et al.,* [19]. They reported that an increase in the thermophoretic and Brownian parameters shows a decline in the Nusselt number. Arshad *et al.,* [20] studied the rate of heat transfer for conventional and hybrid nanofluids, incorporating the Hall Effect over a stretchable surface. The three-dimensional flow of engine oil-based nanofluid under the impact of rotation and partial slip phenomenon over a stretchable surface was examined by Arshad *et al.,* [21]. Zar *et al.,* [22] studied viscous nanofluid flow between parallel plates, as well as the heat and mass transfer, analytically. One of the outcomes of this study shows that the increase in the Prandtl number and the Eckert number will increase the Nusselt number. They reported a decrease in skin friction and a growth in Nusselt number observed for engine oil nanofluid under partial slip parameter as compared to engine oil nanofluid. Jalili *et al.,* [23] investigated electrically conductive Titania nanofluids combined with various base fluids. Arshad *et al.,* [24] assessed the combined influence of the Soret and Dufour effect over dual stretchable porous surfaces considering fluid with nano, hybrid, and tri-hybrid particles. It is reported that improved heat transfer rate and reduced skin friction for triple nanoparticle nanofluids indicate their best performance as compared to the other two nanofluids.

In astrophysical, geophysical, nanotechnological, and engineering problems, magnetohydrodynamic (MHD) flows have become common in recent years. Srinivasacharya and Shiferaw [25] studied Hall and ion-slip current effects for flow in a pipe and reported that Hall and ion-slip parameters result in an increase in both flow velocity and microrotation. A sinusoidally

heated wavy cavity in porous medium nanofluid applied with an inclined magnetic field, studied by Ahmed *et al.,* [26], reported an increase in Hartmann number decreases the Nusselt numbers. For the improvement of heat transfer through dispersion, Nawaz *et al.,* [27] investigated three-dimensional heat transfer in the flow of micro-polar liquid with four types of nanoparticles, taking into account Hall and ion-slip effects using the finite difference method examined by Thomas [28], the finite element method reported by Felippa [29], and the finite volume method presented by Eymard *et al.,* [30], and reported that Hall current enhancement influences the main flow.

The Runge-Kutta method and the finite difference method are widely acknowledged as effective numerical methods for solving differential equations, yet they have their own limitations. The Runge-Kutta method can be computationally expensive, especially for large domains, due to the necessity of evaluating multiple derivatives at each step [31,32]. As the number of steps increases for larger domains, the computational cost grows proportionally. The accuracy of the finite difference method is highly dependent on the chosen grid size [33]. Coarse grids may lead to inaccuracies, while fine grids increase computational costs [34].

In addressing these challenges, the present study introduces the overlapping multi-domain paired quasilinearization method (OMD-PQLM) as an advanced numerical technique for solving highly nonlinear ordinary differential equations (ODEs). The OMD-PQLM enhances computational efficiency and accuracy by integrating spectral collocation methods, which are renowned for their exponential convergence rates when dealing with differential equations with smooth solutions [35]. This characteristic enables the method to achieve high levels of accuracy with fewer grid points, thereby reducing computational costs compared to the finite difference method, which requires finer grids to improve accuracy.

Moreover, the overlapping multi-domain strategy inherent in the OMD-PQLM effectively manages large computational domains and complex boundary conditions. By subdividing the domain into overlapping subdomains, the method ensures the continuity and smoothness of the solution across the entire domain.

These combined features make the OMD-PQLM particularly adept at handling complex, highly nonlinear systems such as those encountered in the study of MHD Williamson-nanofluid flows. The method's ability to maintain high accuracy and computational efficiency over large domains and under varying conditions positions it as a superior alternative to other traditional numerical methods.

This study presents a novel comparative analysis of Williamson and viscous fluids, specifically examining the combined effects of Hall current and Williamson nanofluid flow within a porous medium over a stretching sheet—an area not previously explored in the literature. Additionally, an efficient numerical method (OMD-PQLM) is employed for this investigation.

2. Formulation and Mathematical Description of the Dynamical System

We examine the steady mixed convective, laminar flow of an electrically conducting nanoparticle-immersed Williamson fluid with constant density and volume past a vertically linearly dilating sheet in a porous medium influenced by a perpendicularly applied magnetic field B_0. Additionally, the dynamical system accounts for the effects of Hall current, assuming a small magnetic Reynolds number. The plate is exponentially stretched along the horizontal axis of the three-coordinate system, while the z-axis remains perpendicular to the $x-y$ plane. The mass and momentum conservation equations of the flow are as follows:

$$\nabla \cdot \mathbf{V} = 0, \tag{1}$$

$$(\mathbf{V}\cdot\nabla)\mathbf{V} = \nabla\cdot\mathbf{S} + \rho b. \tag{2}$$

In this context, $\mathbf{V}$ denotes the velocity vector, ρ represents the fluid density, $\mathbf{S}$ stands for the Cauchy stress tensor, and b is the specific body force vector. The definition of the Cauchy stress tensor, $\mathbf{S}$ is as follows:

$$\boldsymbol{S} = -p\mathbf{I} + \tau, \tag{3}$$

and τ is the Williamson fluid model defined as

$$\tau = \left[\mu_\infty + \frac{\mu_0-\mu_\infty}{1-\Gamma\dot{\gamma}}\right]A_1, \tag{4}$$

where $p, I, \tau, \mu_0, \mu_\infty, \Gamma, A_1$ are pressure, identity vector, extra stress tensor, zero viscosity, infinite shear rate viscosity, time constant, and the Rivlin-Erickson tensor, respectively. $\dot{\gamma}$ is given by

$$\dot{\gamma} = \sqrt{\frac{1}{2}\pi}, \quad \text{where} \quad \pi = trace(A_1)^2. \tag{5}$$

In this context, we considered the scenario for which $\mu_\infty = 0$ and $\Gamma\dot{\gamma} \ll 1$. Therefore, τ can be expressed as

$$\tau = \left(\frac{\mu_0}{1-\Gamma\dot{\gamma}}\right)A_1. \tag{6}$$

Through the application of binomial expansion, the expression yields

$$\tau = \mu_0(1+\Gamma\dot{\gamma})A_1. \tag{7}$$

Under the assumptions above and following Nadeem and Akbar [8], and Srinivasacharya and Shiferaw [25], the conservation equations describing the thermal and mass flux in the flow are expressed as:

$$\frac{\partial u}{\partial x} + \frac{\partial v}{\partial y} + \frac{\partial w}{\partial z} = 0, \tag{8}$$

$$u\frac{\partial u}{\partial x} + v\frac{\partial u}{\partial y} + w\frac{\partial u}{\partial z} = \nu\frac{\partial^2 u}{\partial y^2} + \sqrt{2}\Gamma\frac{\partial u}{\partial z}\frac{\partial^2 u}{\partial z^2} - \frac{\nu_f}{k}u - \frac{\sigma B_0^2}{1+\beta^2}(u+\beta v) + g^*[\beta_T(T-T_\infty) + (C-C_\infty)], \tag{9}$$

$$u\frac{\partial v}{\partial x} + v\frac{\partial v}{\partial y} + w\frac{\partial v}{\partial z} = \nu\frac{\partial^2 v}{\partial z^2} + \sqrt{2}\Gamma\frac{\partial v}{\partial z}\frac{\partial^2 v}{\partial z^2} - \frac{\nu}{k}w - \frac{\sigma B_0^2}{1+\beta^2}(\beta u + v), \tag{10}$$

$$u\frac{\partial T}{\partial x} + v\frac{\partial T}{\partial y} + w\frac{\partial T}{\partial z} = \alpha\frac{\partial^2 T}{\partial z^2} + \Lambda\left(D_B\left(\frac{\partial C}{\partial z}\right)\left(\frac{\partial T}{\partial z}\right) + \frac{D_T}{T_\infty}\left(\frac{\partial T}{\partial y}\right)^2\right) + Q(T-T_\infty), \tag{11}$$

$$u\frac{\partial C}{\partial x} + v\frac{\partial C}{\partial y} + w\frac{\partial C}{\partial z} = D_B\frac{\partial^2 C}{\partial z^2} + \frac{D_T}{T_\infty}\frac{\partial^2 T}{\partial z^2} - k_1(C-C_\infty). \tag{12}$$

The boundary conditions are

$$u = U_w, \quad v = V_w, \quad w = 0, \quad T = T_w, \quad C = C_w \text{ at } z = 0, u \to 0, \quad v \to 0, \quad T = T_\infty, \quad C = C_\infty \text{ as } z \to \infty. \tag{13}$$

Here, u, v, w represent the velocity components, β is the Hall parameter, T is the temperature of the nanofluid, γ is the porosity parameter, C is the concentration of nanoparticles, g^* is the gravity, σ is the electric conductivity of the fluid, D_T and B_D are the coefficient of thermophoretic diffusion and Brownian diffusion, $\Lambda = \frac{(\rho C)_p}{(\rho C)_f}$ is the ratio between the effective heat capacity of the nanoparticles and base fluid, k_1 is the chemical reaction, T_∞ and C_∞ ambient temperature and concentration, U_w and V_w are the surface stretching velocities, T_w and C_w are temperature and concentration, and assumed the form

$$U_w = U_0 e^{\frac{x+y}{L}}, \quad V_w = V_0 e^{\frac{x+y}{L}}, \quad T_w = T_\infty + T_0 e^{\frac{A(x+y)}{2L}}, \quad C_w = C_\infty + C_0 e^{\frac{A(x+y)}{2L}},$$

where U_0, V_0, T_0, C_0 are constants, and L is the reference length.

Applying the following group of similarity transformations

$$u = U_0 e^{\frac{x+y}{L}} g'(\eta), v = V_0 e^{\frac{x+y}{L}} h'(\eta), w = \left(\frac{U_0}{2\nu L}\right)^{1/2} e^{\frac{x+y}{2L}} (g' + \eta g' + h + \eta h'),$$
$$T = T_\infty + T_0 e^{\frac{x+y}{2L}} \omega(\eta), \approx C = C_\infty + C_0 e^{\frac{x+y}{2L}} \theta(\eta), \approx \eta = z\sqrt{\frac{U_0}{2\nu L}}, \tag{14}$$

and substituting Eq. (14) into Eq. (8) to Eq. (12), we get the following non-dimensional system of equations:

$$(1 + \chi g'')g''' + (g + h)g'' - 2(g' + h)g' + \lambda(\omega + N_r\theta) - \gamma g' - \frac{M}{1+\beta^2}(g' + \beta h') = 0, \tag{15}$$

$$(1 + \chi h')h''' + (g + h)h'' - 2(g' + h')h' - \gamma h' - \frac{M}{1+\beta^2}(\beta g' - h') = 0, \tag{16}$$

$$\omega'' + Pr[(g + h)\omega' - A(g' + h')\omega + Nb\omega'\theta' + Nt\omega'^2] + Q\omega = 0, \tag{17}$$

$$\theta'' + PrLe[(g + h)\theta' - A(g' + h')\theta] + \frac{N_t}{N_b}\omega'' - K\theta = 0, \tag{18}$$

where $\chi = \Gamma U_0\sqrt{\frac{U_w}{\nu L}}$ is the Williamson parameter, $G_r = \frac{h^*\beta_T(T_w - T_\infty)x^3}{\nu^2}$ is the temperature Grashof number, $Re_x = \frac{U_0 L}{\nu} e^{\frac{x+y}{L}}$ is the Reynolds number, $\lambda = \frac{G_r}{Re^2}$ is the mixed convection parameter, $M = \frac{2L\sigma B_0^2}{U_w\rho}$ is the magnetic parameter, $\gamma = \frac{\nu_f}{Ka}$ is the porosity parameter, $Nr = \frac{\beta_c(C_w - C_\infty)}{\beta_T(T_w - T_\infty)}$ is the buoyancy ratio parameter, $Nb = \frac{\Lambda D_B(C_w - C_\infty)}{\nu_f}$ is the Brownian motion parameter, $Nt = \frac{\Lambda D_T(T_w - T_\infty)}{T_\infty \nu}$ is the thermophoresis parameter, $Pr = \frac{\nu}{\alpha}$ is the Prandtl number, $K = \frac{2k_1}{U_w}$ is the chemical reaction parameter and $Le = \frac{\alpha}{D_B}$ is the Lewis number.

The boundary conditions now take the form:

$$g = 0, \quad g' = 1, \quad h = 0, \quad h' = S, \quad \omega = 1 \quad \theta = 1, \quad \text{at} \quad \eta = 0,$$

$$g' \to 0, \quad h' \to 0, \quad \omega \to 0 \quad \theta \to 0, \quad \text{as} \quad \eta \to \infty, \tag{19}$$

where $S = \frac{V_0}{U_0}$ is the stretching ratio.

The engineering parameters of interest are the Skin friction coefficients C_{fx} and C_{fy} , the Sherwood number Sh_x , and the local Nusselt number Nu_x given by

$$C_{fx} = \frac{\tau_{ux}}{\rho U_w^2}, \quad C_{fy} = \frac{\tau_{wy}}{\rho U_w^2}, \quad Nu_x = \frac{x q_w}{k(T_w - T_\infty)}, \qquad Sh_x = \frac{x q_m}{D_B(C_w - C_\infty)}, \tag{20}$$

where

$$\tau_{ux} = \mu\left(\frac{\partial u}{\partial z} + \frac{\Gamma}{\sqrt{2}}\left(\frac{\partial u}{\partial z}\right)^2\right)_{z=0}, \quad \tau_{wy} = \mu\left(\frac{\partial w}{\partial y} + \frac{\Gamma}{\sqrt{2}}\left(\frac{\partial w}{\partial y}\right)^2\right)_{z=0},$$

$$q_w = -k\left(\frac{\partial T}{\partial z}\right)_{z=0}, \quad q_m = -D_B\left(\frac{\partial C}{\partial z}\right)_{z=0}. \tag{21}$$

The non-dimensional form is written as

$$Re_x^{1/2} C_{fx} = g''(0) + \frac{\chi}{2} g''^2(0), \quad Re_x^{1/2} C_{fy} = h''(0) + \frac{\chi}{2} h''^2(0),$$

$$Re_x^{-1/2} Nu_x = \omega'(0), \quad Re_x^{-1/2} Sh_x = \theta'(0) \tag{22}$$

3. Description of the OMD-PQLM

This section outlines the implementation of the OMD-PQLM for a general system of ODEs comprising M equations with M unknowns. We consider an ODE given by the following:

$$[v_1(\alpha)] = 0, \quad \alpha \in [\alpha_0, \alpha_f], \tag{23}$$

where v is the set of the unknown function and its spatial domain defined as

$$\boldsymbol{v_1} = \left\{v_1, \frac{dv_1}{d\alpha}, \dots, \frac{d^{h-1}v_1}{d\alpha^{h-1}}, \frac{d^h v_1}{d\alpha^h}\right\}, \tag{24}$$

with h being the highest derivative.

Further consideration involves a system of M ODEs in M unknowns, given as

$$\boldsymbol{G}_l[\boldsymbol{v}_1(\alpha), \boldsymbol{v}_2(\alpha), \dots, \boldsymbol{v}_M(\alpha)] = 0, \quad l = 1,2, \dots, M, \tag{25}$$

signifies a coupled system of non-linear ODEs, $\boldsymbol{G}_l$ represents a non-linear operator for each equation for $l = 1, \cdots, M$ and $\{v_1, v_2, \dots, v_M\}$ is a set that contains

$$\left[\left\{v_1^{(0)}, v_1^{(1)}, \dots, v_1^{(h_1)}\right\}, \dots, \left\{v_M^{(0)}, v_M^{(1)}, \dots, v_M^{(h_M)}\right\}\right].$$

3.1 Paired Quasilinearization Method

To solve the general system (25), we implement the PQLM [35,36]. Although random combinations can also be used for pairing, an ordered pairing will be used to demonstrate how the PQLM is implemented. Assume that v_1 and v_2 are the first pairing. To obtain a linearized pair, the quasilinearization is applied to equations $G_1(v_1, v_2, \cdots, v_M)$ and $G_2(v_1, v_2, \cdots, v_M)$. Similarly, the process is applied for successive pairs, incorporating improved solutions from preceding pairs to iteratively update the succeeding pairs. Generally, the pairing assumes the following structure:

$$G_w[v_1, \cdots, v_M] = 0, \quad w = \{\{1,2\},\{3,4\}, \dots, \{M-1, M\}\}. \tag{26}$$

3.2 Overlapping Grids

The interval of integration $[\alpha_0, \alpha_f]$ is partitioned using an overlapping approach into z overlapping sub-domains, each of length L_α represented as [37]

$$I_\psi = \left[x_0^\psi, x_{Nx}^\psi\right] \quad \psi = 1,2,3, \dots, z. \tag{27}$$

The interval is then discretized into a set of $N_\alpha + 1$ collocation points. Within the I_ψ subinterval, the last two points overlap with the initial two points of the subsequent $I_{\psi+1}$ subinterval. The subinterval's length is consistently defined as

$$L_\alpha = \frac{\alpha_f - \alpha_0}{z + \frac{1}{2}(1-z)\left(1 - cos\frac{\pi}{N_\alpha}\right)}, \tag{28}$$

We observe that the domain's total length is given by

$$\alpha_f - \alpha_0 = 2L_\alpha - \rho + (2L_\alpha - 2\rho)\left(\frac{z}{2} - 1\right) = 2L_\alpha - \rho + (L_\alpha - \rho)(z-2). \tag{29}$$

Eq. (29) is used to derive the formula in Eq. (28), where the parameter ρ represent the overlapping distance.

Figure 1 displays the overlapping grid on the spatial domain. Focusing on the initial interval I_1, where $\alpha \in [\alpha_0, x_{N_\alpha}^1]$ and the length $L_\alpha = x_{N_\alpha}^1 - \alpha_0$, the application of the linear transformation $x = \frac{L_\alpha}{2}\zeta + \frac{\alpha_0 + x_{N_x}^1}{2}$ facilitates the conversion of the interval $[\alpha_0, x_{N_\alpha}^1]$ into the standardized form $[-1,1]$.

Consequently, using the Gauss-Lobatto collocation points $\zeta_m = \cos\left(\frac{\pi m}{N_\alpha}\right)$, where $m = 0,1,2,3, \dots, N_\alpha$, we derive

$$\rho = \frac{L_\alpha}{2}(\zeta_0 - \zeta_1) = \frac{L_\alpha}{2}\left(1 - cos\frac{\pi}{N_\alpha}\right). \tag{30}$$

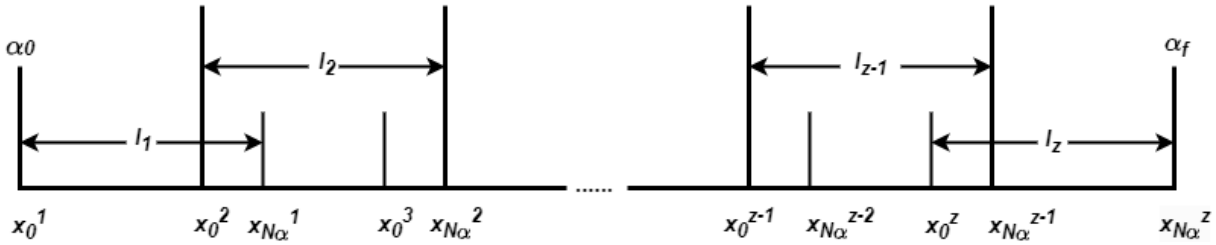

Fig. 1. Overlapping grid on the spatial domain

As a result, Eq. (29) transforms to

$$\alpha_f - \alpha_0 = \rho(1-z) + zL_\alpha = \frac{L_\alpha}{2}\left(1 - cos\frac{\pi}{N_\alpha}\right)(1-z) + zL_\alpha. \tag{31}$$

Upon rearrangement, with L_α as the subject, it yields Eq. (28). Prior to utilizing the spectral collocation technique within each distinct subinterval, the interval I_ψ is converted to $\zeta \in [-1,1]$ using

$$x_m^\psi = \frac{x_{N_\alpha}^\psi - x_0^\psi}{2}\zeta + \frac{x_{N_\alpha}^\psi + x_0^\psi}{2}, \quad \{\zeta_m\}_{m=0}^{N_\alpha} = \cos\left(\frac{\pi m}{N_\alpha}\right). \tag{32}$$

3.3 Spectral Collocation Methods

This section shows the implementation of the Chebyshev spectral collocation technique on the linearized pairs of equations. We have the overlapping interval I_ψ linearly transformed into $\zeta \in [-1,1]$. The process of determining solutions to the linearized pairs of equations involves utilizing Lagrange interpolation polynomials in the following form

$$\begin{aligned} v_1(\zeta) &\approx \textstyle\sum_{m=0}^{N_\alpha} v_1(\zeta_m)L_m(\zeta), \\ v_2(\zeta) &\approx \textstyle\sum_{m=0}^{N_\alpha} v_2(\zeta_m)L_m(\zeta), \\ &\vdots \\ v_M(\zeta) &\approx \textstyle\sum_{m=0}^{N_\alpha} v_M(\zeta_m)L_m(\zeta), \end{aligned} \tag{33}$$

L_m signify the Lagrange cardinal function given by

$$L_m(\zeta) = \prod_{m=0, m\neq w}^{N_\alpha} \frac{\zeta - \zeta_w}{\zeta_m - \zeta_w}. \tag{34}$$

The grid points used are Chebyshev-Gauss-Lobatto points, denoted by ζ_m as shown in Eq. (35).

$$\zeta_m = cos\frac{\pi m}{N_\alpha}, \quad m = 0,1,\dots,N_\alpha, \tag{35}$$

The differentiation matrix $\overline{\overline{D}}$, as per Trefethen [38] is transformed just as the domain is transformed. The transformed differentiation matrix takes the form

$$\mathbf{D} = \frac{2}{L_\alpha}\overline{\overline{D}}, \tag{36}$$

The linearized pairs of equations are solved by implementing the Chebyshev spectral collocation approach with an overlapping approach.

4. Numerical Discretization of the Fluid Flow System

This section describes the application of the OMD-PQLM as detailed in Section 3 to solve the system of non-linear Eq. (15) to Eq. (18). There are three different ways to pair the systems of Eq. (15) to Eq. (18). These combinations will be considered to determine how the various sets of pairing affect the speed of convergence and solutions. The pairings are defined as follows:

i. case 1: involves the pairings ($\{g, h\}$ and $\{\omega, \theta\}$) corresponding to the Eq. (15), Eq. (16) and Eq. (17), Eq. (18),
ii. case 2: involves the pairings ($\{g, \omega\}$ and $\{h, \theta\}$) corresponding to the Eq. (15), Eq. (17) and Eq. (16), Eq. (18) and
iii. case 3: involves the pairings ($\{g, \theta\}$ and $\{g, \omega\}$) corresponding to the Eq. (15), Eq. (18) and Eq. (16), Eq. (17).

4.1 Case 1: Involves the Pairings ($\{g, h\}$ and $\{\omega, \theta\}$) Corresponding to the Eq. (15), Eq. (16) and Eq. (17), Eq. (18)

The Taylor series expansion of first order is used to linearize the non-linear components $\chi g'' g''', g g'', h g'', -2g'^2, -2hg',\ \chi h' h''', (g+h)h''$, and $-2(g'+h')h'$ in order to obtain the linearized combination

$$(1+\chi g_r'')g_{r+1}''' + (\chi g_r''' + g_r + h_r)g_{r+1}'' + \left(-4g_r' - 2h_r' - \gamma - \frac{M}{1+\beta^2}\right)g_{r+1}' + (g_r'')g_{r+1} + \left(-2g_r' + \frac{M\beta}{1+\beta^2}\right)h_{r+1}' + (g_r'')h_{r+1} = \chi g_r'' g_r''' + (g_r + h_r)g_r'' - 2(g_r' + h_r')g_r' - \lambda(\omega_r + N_r\theta_r), \quad (37)$$

$$\left(-2h_r' - \frac{M\beta}{1+\beta^2}\right)g_{r+1}' + (h_r'')g_{r+1} + (1+\chi h_r')h_{r+1}''' + (g_r + h_r)h_{r+1}'' + \left(\chi h_r''' - 2g_r' - 4h_r' - \gamma - \frac{M}{1+\beta^2}\right)h_{r+1}' + (h_r'')h_{r+1} = \chi h_r' h_r''' + (g_r + h_r)h_r'' - 2(g_r' + h_r')h_r'. \quad (38)$$

The Chebyshev spectral collocation and overlapping approaches are then applied to the linearized pair in the following manner:

$$\left[[a_0]\mathbf{D}^3 + [a_1]\mathbf{D}^2 + [a_2]\mathbf{D} + g_r''\right]\mathbf{G}_{r+1} + \left[[a_3]\mathbf{D} + g_r''\right]\mathbf{H}_{r+1} = \boldsymbol{R}_1, \quad (39)$$

$$\left[[b_0]\mathbf{D} + [b_1]\right]\mathbf{G}_{r+1} + \left[[b_2]\mathbf{D}^3 + [b_3]\mathbf{D}^2 + [b_4]\mathbf{D} + g_r''\right]\mathbf{H}_{r+1} = R_2, \quad (40)$$

where

$$a_0 = 1 + \chi g_r'', \quad a_1 = \chi g_r''' + g_r + h_r, \quad a_2 = -4g_r' - 2h_r' - \gamma - \frac{M}{1+\beta^2}, \quad a_3 = g_r'',$$

$$a_4 = -2g_r' + \frac{M\beta}{1+\beta^2}, \quad b_0 = -2h_r' - \frac{M\beta}{1+\beta^2}, \quad b_1 = h_r'', \quad b_2 = 1 + \chi h_r',$$

$$b_3 = g_r + h_r, \quad b_4 = \chi h_r''' - 2g_r' - 4h_r' - \gamma - \frac{M}{1+\beta^2},$$

$$R_1 = \chi g_r'' g_r''' + (g_r + h_r) g_r'' - 2(g_r' + h_r) g_r' - \lambda(\omega_r + N_r \theta_r),$$

$$R_2 = \chi h_r' h_r''' + (g_r + h_r) h_r'' - 2(g_r' + h_r') h_r'.$$

The second set of equations integrates the revised solutions for g and h. The linearized pair is obtained by linearizing the non-linear components, $PrNb\omega'\theta'$ and $PrNt\omega'^2$ using the first-order Taylor series expansion.

$$\omega_{r+1}'' + Pr\big((g_r + h_r) + Nb\theta_r + 2Nt\omega_r'\big)\omega_{r+1}' + \big(Pr\big(-A(g_r' + h_r')\big) + Q\big)\omega_{r+1} + [PrNb\omega_r']\theta_{r+1}' = PrNb\omega_r'\theta_r' + PrNt\omega_r'^2, \quad (41)$$

$$\left(\frac{Nt}{Nb}\right)\omega_{r+1}'' + \theta_{r+1}'' + \big(PrLe(g_r + h_r)\big)\theta_{r+1}' + \big(PrLe\big(-A(g_r' + h_r')\big) - K\big)\theta_{r+1} = 0. \quad (42)$$

The Chebyshev spectral collocation method and the overlapping approach are applied in the following manner:

$$\big[\mathbf{D}^2 + [c_0]\mathbf{D} + [c_1]\big]\mathbf{\Omega}_{r+1} + \big[[c_2]\mathbf{D}\big]\mathbf{\Theta}_{r+1} = R_3, \quad (43)$$

$$\left[\left(\frac{N_t}{Nb}\right)\mathbf{D}^2\right]\mathbf{\Omega}_{r+1} + \big[\mathbf{D}^2 + [e_0]\mathbf{D} + [e_1]\big]\mathbf{\Theta}_{r+1} = R_4, \quad (44)$$

where

$$c_0 = Pr[(g_r + h_r) + Nb\theta_r' + 2Nt\omega_r'], \quad c_1 = Pr\big(-A(g_r' + h_r')\big) + Q, \quad c_2 = PrNb\omega_r'$$

$$e_0 = PrLe(g_r + h_r), \quad e_1 = PrLe\big(-A(g_r' + h_r')\big) - K,$$

$$R_3 = PrNb\omega_r'\theta_r' + PrNt\omega_r'^2, \quad R_4 = 0.$$

4.2 Case 2: Involves the Pairings $(\{g, \omega\}$ *and* $\{h, \theta\})$ *Corresponding to the Eq. (15), Eq. (17) and Eq. (16), Eq. (18)*

The linearized pair is obtained by linearizing the non-linear components, $\chi g'' g'''$, gg'', $-2g'^2$, and $Pr(g\omega' - Ag'\omega - Nt\omega'^2)$, by the use of the first-order Taylor series expansion. The Chebyshev spectral collocation and overlapping approaches are then applied in the following manner:

$$\big[[a_0]\mathbf{D}^3 + [a_1]\mathbf{D}^2 + [a_2]\mathbf{D} + f_r''\big]\mathbf{G}_{r+1} + [\lambda]\mathbf{\Omega}_{r+1} = R_1, \quad (45)$$

$$\big[[b_0]\mathbf{D} + [b_1]\big]\mathbf{G}_{r+1} + \big[\mathbf{D}^2 + [b_2]\mathbf{D} + [b_3]\big]\mathbf{\Omega}_{r+1} = R_1, \quad (46)$$

where

$$a_0 = 1 + \chi g_r'', \quad a_1 = \chi g_r''' + g_r + h_r, \quad a_2 = -4g_r' - 2h_r - \gamma - \frac{M}{1+\beta^2}, \quad a_3 = f_r'',$$

$$b_0 = -PrA\omega_r, \quad b_1 = Pr\omega_r', \quad b_2 = Pr(g_r + h_r + Nb\theta_r' + 2Nt\omega_r'),$$

$b_3 = -PrA(g_r' + h_r') + Q,$

$R_1 = \chi g_r'' g_r''' + g_r g_r'' - 2g_r'^2 - \lambda Nr\theta_r + \frac{M\beta h_r'}{1+\beta^2},$

$R_2 = Pr(g_r\omega_r' - Ag_r'\omega_r + Nt\omega_r'^2).$

The second set of equations integrates the revised solutions for g and ω. The linearized pair is obtained by linearizing the non-linear components, $\chi h'h'', hh'', PrLe(h\theta' - Ah'\theta)$, and h'^2, using the first-order Taylor series expansion. The Chebyshev spectral collocation and overlapping approaches are then applied in the following manner:

$$\left[[c_0]\mathbf{D}^3 + [c_1]\mathbf{D}^2 + [c_2]\mathbf{D} + h_r''\right]\mathbf{H}_{r+1} + [0]\mathbf{\Theta}_{r+1} = R_3, \quad (47)$$

$$\left[[e_0]\mathbf{D} + [e_1]\right]\mathbf{H}_{r+1} + \left[\mathbf{D}^2 + [e_2]\mathbf{D} + [e_3]\right]\mathbf{\Theta}_{r+1} = R_4, \quad (48)$$

where

$c_0 = 1 + \chi h_r', \quad c_1 = g_{r+1} + h_r, \quad c_2 = \chi h_r'' - 4h_r' - 2g_{r+1}' - \gamma - \frac{M}{1+\beta^2},$

$e_0 = PrLe(-A\omega_{r+1}), \quad e_1 = PrLe\theta_r', \quad e_2 = PrLe(g_{r+1} + h_r),$

$e_3 = PrLe\left(-A(g_{r+1}' + hr')\right) - k,$

$R_3 = \chi h_r' h_r''' + h_r h_r'' - 2h_r^2 + \frac{M\beta g_{r+1}'}{1+\beta^2},$

$R_3 = PrLe(h_r\theta_r' - Ah_r'\theta_r) - \frac{Nt}{Nb}\omega_{r+1}''.$

4.3 Case 3: Involves the Pairings ($\{g, \theta\}$ and $\{h, \omega\}$) Corresponding to the Eq. (15), Eq. (18) and Eq. (16), Eq. (17)

The linearized pair is obtained by linearizing the non-linear components, and $\chi g''g''', gg'', hg'', -2g'^2$, and $PrLe(g\theta' - Ag'\theta)$ by the use of the first-order Taylor series expansion. The Chebyshev spectral collocation and overlapping approaches are then applied in the following manner:

$$\left[[a_0]\mathbf{D}^3 + [a_1]\mathbf{D}^2 + [a_2]\mathbf{D} + g_r''\right]\mathbf{G}_{r+1} + [\lambda Nr]\mathbf{\Theta}_{r+1} = R_1, \quad (49)$$

$$\left[[b_0]\mathbf{D} + [b_1]\right]\mathbf{G}_{r+1} + \left[\mathbf{D}^2 + [b_2]\mathbf{D} + [b_3]\right]\mathbf{\Theta}_{r+1} = R_2, \quad (50)$$

where

$a_0 = 1 + xg_r'', \quad a_1 = \chi g_r''' + g_r h_r, \quad a_2 = -4g_r' - 2h_r' - \gamma - \frac{M}{1+\beta^2},$

$b_0 = -PrLeA\theta_r, \quad b_1 = PrLe\theta_r', \quad b_2 = PrLe(g_r + h_r),$

$$b_3 = -PrLeA(g_r' + h_r') - k,$$

$$R_1 = \chi g_r'' g_r''' + g_r g_r'' - 2g_r'^2 - \lambda\omega_r - \frac{M\beta h_r'}{1+\beta^2},$$

$$R_2 = PrLe(g_r\theta_r' - Ag_r'\theta_r) - \frac{Nt}{Nb}\omega_r''.$$

The subsequent pair of equations make use of the improved solutions for g and θ. The linearized pair is obtained by linearizing the non-linear components, $\chi h'h''$, hh'', and h'', using the first-order Taylor series expansion. The linearized system is solved using the Chebyshev spectral collocation and overlapping approaches as follows:

$$\left[[c_0]\mathbf{D}^3 + [c_1]\mathbf{D}^2 + [c_2]\mathbf{D} + h_r''\right]\mathbf{H}_{r+1} + [\mathbf{0}]\mathbf{\Omega}_{r+1} = R_1, \tag{51}$$

$$\left[[e_0]\mathbf{D} + [e_1]\right]\mathbf{H}_{r+1} + \left[\mathbf{D}^2 + [e_2]\mathbf{D} + [e_3]\right]\mathbf{\Omega}_{r+1} = R_2, \tag{52}$$

where

$$c_0 = 1 + xh_r', \quad c_1 = g_{r+1} + h_r, \quad c_2 = \chi h_{r+1}''' - 4h_r' - 2f_{r+1}' - \gamma - \frac{M}{1+p^2},$$

$$e_0 = -PrA\omega_r, \quad e_1 = Pr(\omega_r'), \quad e_2 = Pr(g_{r+1} + h_r) + Nt\theta_{r+1}' + 2Nt\omega_r$$

$$e_3 = Pr(-A(g_{r+1}' - Ah_r') + Q)$$

$$R_3 = Xh_r'h_r''' + h_r h_r'' - 2h_r'^2 + \frac{M\beta g_{r+1}'}{1+\beta^2}$$

$$R_4 = Pr(g_r\omega_r' - Ah_r'\omega_r + A_t\omega_r'^2)$$

5. Findings and Analysis

The numerical solution of Eq. (15) to Eq. (18), along with the boundary conditions in Eq. (19) is obtained using the OMD-PQLM and the PQLM. Unless otherwise specified, the values of the constants and intervals for the numerical simulations are defined as follows: $0 \le \chi \le 4, 1 \le \lambda \le 6, 1 \le K \le 6$, $2 \le M \le 6$, and for the numerical simulations $\chi = 0.3, \lambda = Nb = Nt = Q = Le = 0.5, Nr = \gamma = K = 1, M = 3, \beta = 2$ and $Pr = A = 5$. Convergent results were achieved using 50 grid points for the PQLM and 15 grid points for the OMD-PQLM. The number of overlapping sub-intervals was set to 6, and the domain was defined as $[0,20]$.

The analysis of the solution error is undertaken to analyze the convergence. The solution error is determined by computing the norm of the difference of two consecutive iterations of the approximate solutions.

The errors in solutions for Eq. (15) to Eq. (18) can be observed in Figure 2 to Figure 5. It is noted that as the number of iterations increases, the error between two successive approximate solutions decreases until it reaches a point beyond in which further improvement is not possible. When the error reaches its minimum and can no longer decrease, it indicates that the method has converged. The OMD-PQLM cases demonstrate the smallest error in solutions, whereas the PQLM cases attain convergence more quickly than the OMD-PQLM cases. Both Case 1 of the PQLM and the OMD-PQLM

exhibit rapid convergence, as evidenced by the steep incline of the slope. In both Case 1 of the PQLM and the OMD-PQLM, the solution errors for $g(\eta)$, $h(\eta)$, $\omega(\eta)$, and $\theta(\eta)$ exhibit convergence between the 8^{th} and 12^{th} iterations. The OMD-PQLM cases exhibit all desirable characteristics and demonstrate rapid convergence with a higher level of accuracy in comparison to other cases.

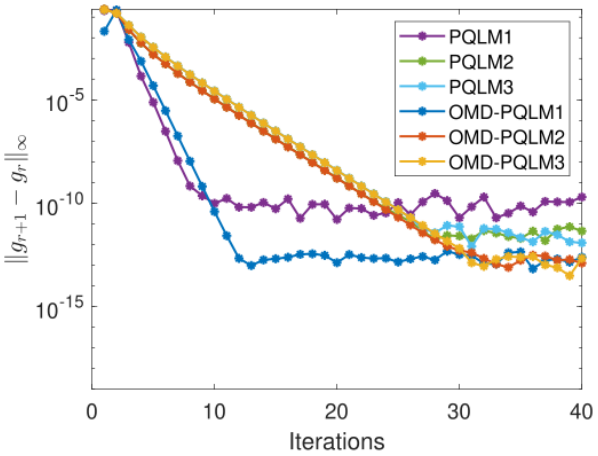

Fig. 2. Error in $\boldsymbol{g}$ between consecutive iterations

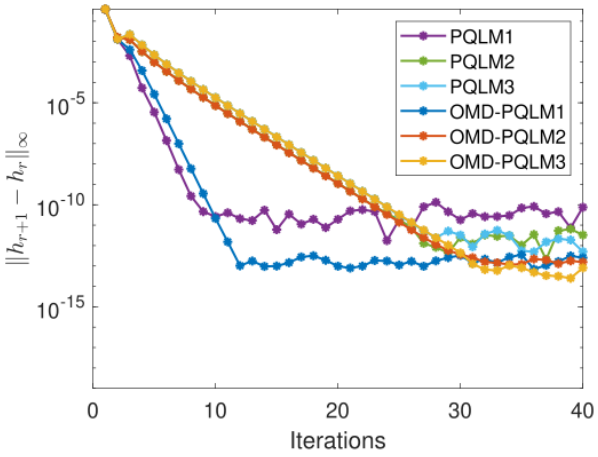

Fig. 3. Error in h between consecutive iterations

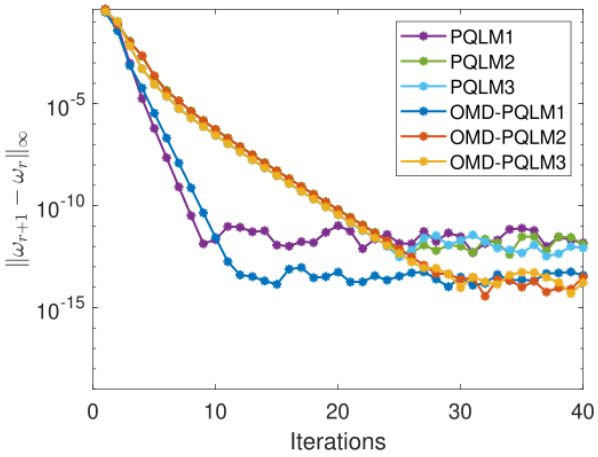

Fig. 4. Error in $\boldsymbol{\omega}$ between consecutive iterations

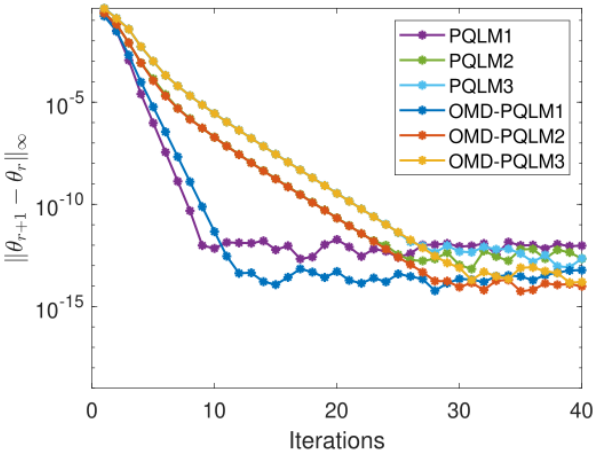

Fig. 5. Error in g between consecutive iterations

The estimated solutions obtained through the OMD-PQLM are then substituted into the transformed model equations to obtain the residual norm, in the following manner:

$$Res(\boldsymbol{G}) = (1+\chi\boldsymbol{g}'')\boldsymbol{g}''' + (\boldsymbol{g}+\boldsymbol{h})\boldsymbol{g}'' - 2(\boldsymbol{g}'+\boldsymbol{h})\boldsymbol{g}' + \lambda(\omega + N_r\boldsymbol{\theta}) - \gamma\boldsymbol{g}' + \frac{M}{1+\beta^2}(\boldsymbol{g}' + \beta\boldsymbol{h}'), \quad (53)$$

$$Res(\boldsymbol{H}) = (1+\chi\boldsymbol{h}')\boldsymbol{h}''' + (\boldsymbol{g}+\boldsymbol{h})\boldsymbol{h}'' - 2(\boldsymbol{g}'+\boldsymbol{h}')\boldsymbol{h}' - \gamma\boldsymbol{h}' - \frac{M}{1+\beta^2}(\beta\boldsymbol{g}' - \boldsymbol{h}'), \quad (54)$$

$$Res(\boldsymbol{\Omega}) = \boldsymbol{\omega}'' + Pr\left[(\boldsymbol{g}+\boldsymbol{h})\boldsymbol{\omega}' - A(\boldsymbol{g}'+\boldsymbol{h}')\boldsymbol{\omega} + Nb\boldsymbol{\omega}'\boldsymbol{\theta}' + Nt\boldsymbol{\omega}'^2\right] + Q\boldsymbol{\omega}, \quad (55)$$

$$Res(\boldsymbol{\Theta}) = \boldsymbol{\theta}'' + PrLe[(\boldsymbol{g}+\boldsymbol{h})\boldsymbol{\theta}' - A(\boldsymbol{g}'+\boldsymbol{h}')\boldsymbol{\theta}] + \frac{N_t}{N_b}\boldsymbol{\omega}'' - K\boldsymbol{\theta}. \quad (56)$$

Figure 6 to Figure 9 show the effect of the number of iterations on accuracy. As the number of iterations increases, it is noteworthy that the accuracy for Figure 6 to Figure 8 improves until it

reaches an optimum level beyond in which it cannot be further improved. The OMD-PQLM cases exhibit higher accuracy compared to all the PQLM cases. While the PQLM cases converge faster, they reach a lower accuracy compared to the OMD-PQLM cases. Specifically, Case 1 of the PQLM demonstrates the fastest convergence but achieves the lowest accuracy level, with the residual error for $h(\eta)$ being the highest among the cases. Conversely, OMD-PQLM Case 1 embodies all desirable characteristics, demonstrating both higher accuracy and faster convergence. The residual errors for the OMD-PQLM fall within the range of 10^{-13} to 10^{-14}, indicating that the OMD-PQLM is highly effective in solving similar problems discussed in this study. The OMD-PQLM Case 1 was used to carry out the analysis of different parameters of interest since it embodies both higher accuracy and faster convergence.

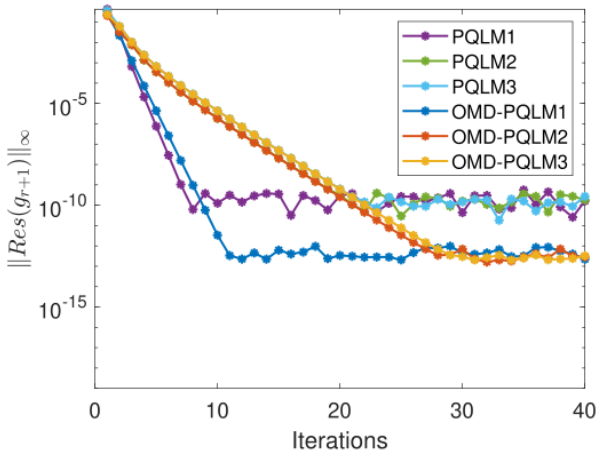

Fig. 6. The impact of iterations on $|Res(g)|_\infty$

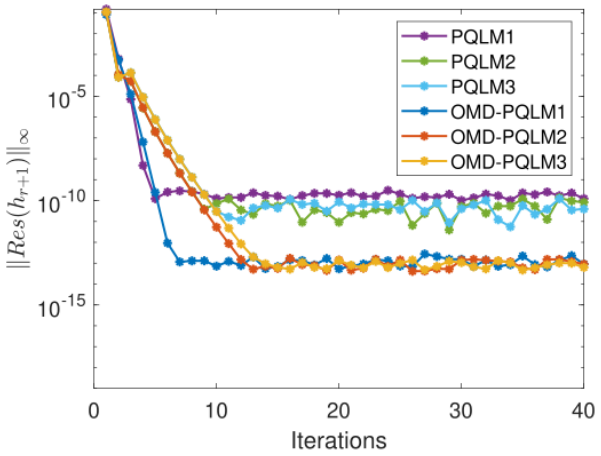

Fig. 7. The impact of iterations on $|\boldsymbol{Res(h)}|_\infty$

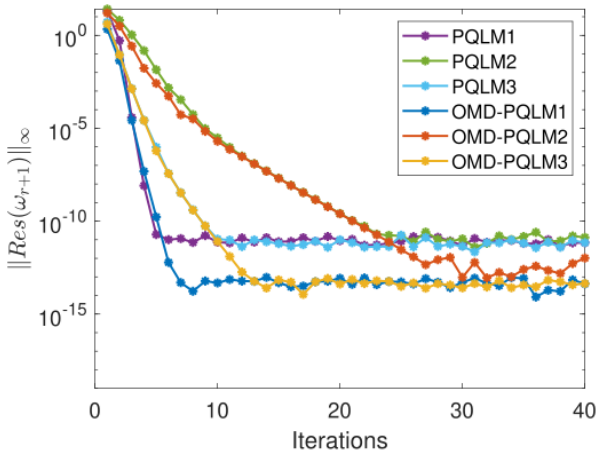

Fig. 8. The impact of iterations on $|Res(\omega)|_\infty$

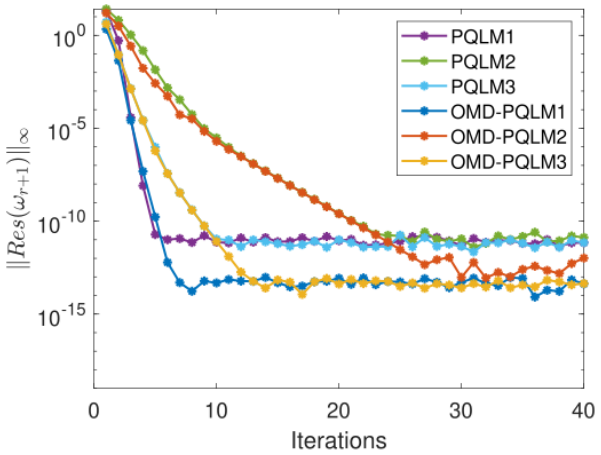

Fig. 9. The impact of iterations on $|Res(\theta)|_\infty$

The behaviour of χ, β, N_t and N_b on $-Cf_x, -Cf_y, -Nu_x$ and $-Sh_x$ is investigated in Table 1. The data regarding the impact of these parameters on the physical quantities is thoroughly presented in Table 1 for the reader's reference.

Table 1
Various parameters on wall shear stresses, Nusselt number and mass diffusion rate when $\boldsymbol{\lambda = 0.5, M = 3, \gamma = 1, Pr = 5, A = 5, Q = 0.5, Le = 0.5}$ and $\boldsymbol{K = 1}$

χ	β	N_t	N_b	$-Cf_x$	$-Cf_y$	$-Nu_x$	$-Sh_x$
0	2	0.5	0.6	0.67742	0.67871	2.19572	1.34269
0.2	2	0.5	0.6	0.63707	0.56628	2.18050	1.34258
0.4	2	0.5	0.6	0.58182	0.46753	2.15524	1.33959
0.4	1	0.5	0.6	0.62270	0.49491	2.01304	1.34239
0.4	2	0.5	0.6	0.58182	0.46753	2.15524	1.33958
0.4	2	0.5	0.6	0.56216	0.43742	2.23207	1.33217
0.4	2	0.1	0.6	0.59379	0.46235	2.48693	1.59642
0.4	2	0.5	0.6	0.58182	0.46753	2.15524	1.33959
0.4	2	0.8	0.6	0.57403	0.47121	1.96815	1.21695
0.4	2	0.5	0.1	0.52480	0.48354	−3.48275	2.27848
0.4	2	0.5	0.4	0.57862	0.46880	1.66283	1.63501
0.4	2	0.5	0.7	0.58217	0.46733	2.27932	1.22084

5.1 Combined Effects of the Williamson and Hall Parameters

Figure 10 to Figure 13 show the combined effects of the Hall and Williamson parameters on the flows' velocities in the x and y directions, $g'(\eta)$ and $h'(\eta)$, the concentration, $\theta(\eta)$, and the temperature distribution, $\omega(\eta)$. The Williamson parameter significantly influences the flows' velocities, temperature distribution, and concentration. It is observed that both $g'(\eta)$ and $h'(\eta)$ increase as the Hall parameter, β, increases, indicating heightened velocity components in the x and y directions. When the Hall parameter increases, it indicates a stronger dominance of electromagnetic effects relative to the viscous effects in the flow. The Lorentz force, which arises due to the interaction between the magnetic field and the electrically conducting fluid, can exert an acceleration effect on the fluid particles, causing them to move with higher velocities. When the Williamson parameter, χ, is set to $0.4, g'(\eta)$ consistently remain below the case of a viscous fluid $(\chi = 0)$. For $h'(\eta)$, with $\chi = 0$, the velocity in the $y-$direction consistently remains lower compared to $\chi = 0.4$, implying that the shear-thinning effects enhance the speed in the $y-$direction. As the Hall parameter, β, increases, the temperature distribution, $\omega(\eta)$, and concentration, $\theta(\eta)$, both decreases, showing an inverse relationship. The evidence suggests that a larger β value lead to a cooling impact and modifies the behaviour of nanoparticles within the nanofluid. In the absence of the Williamson parameter, lower temperatures and concentrations are constantly observed, suggesting that the shear-thinning property of the Williamson parameter leads to an increased concentration and temperature.

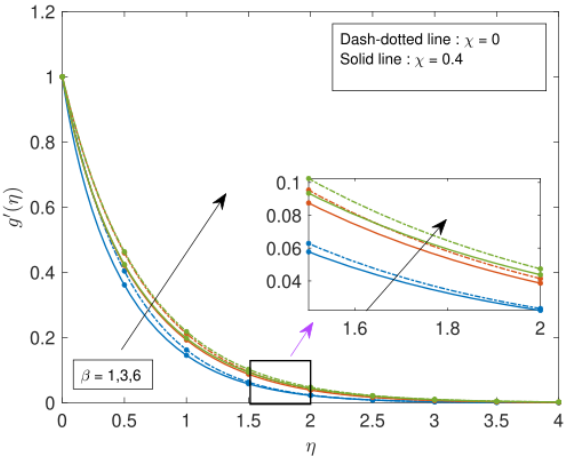

Fig. 10. Impact of the Williamson parameter, χ, and the Hall parameter, β, on $g'(\eta)$

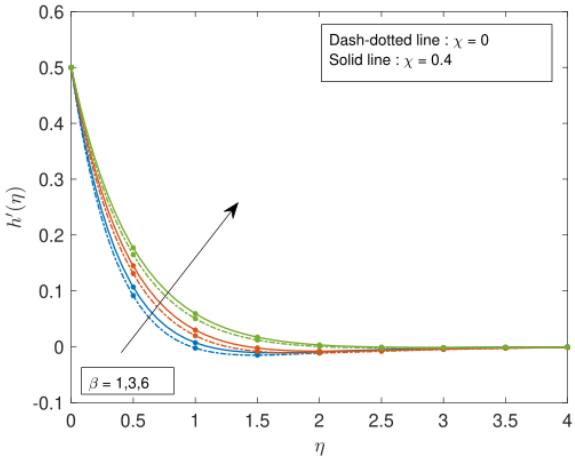

Fig. 11. Impact of the Williamson parameter, χ, and the Hall parameter, β, on $h'(\eta)$

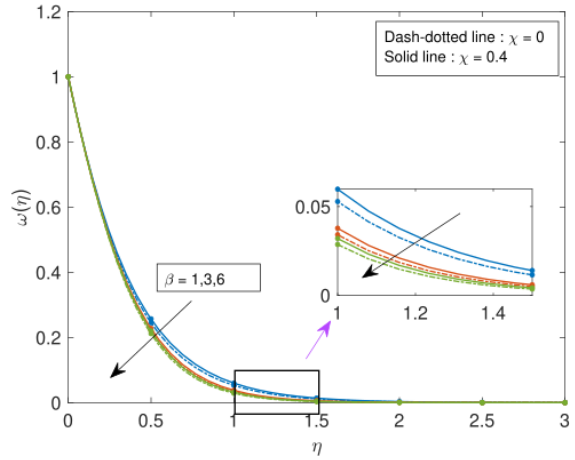

Fig. 12. Impact of the Williamson parameter, **χ**, and the Hall parameter, **β**, on $\boldsymbol{\omega(\eta)}$

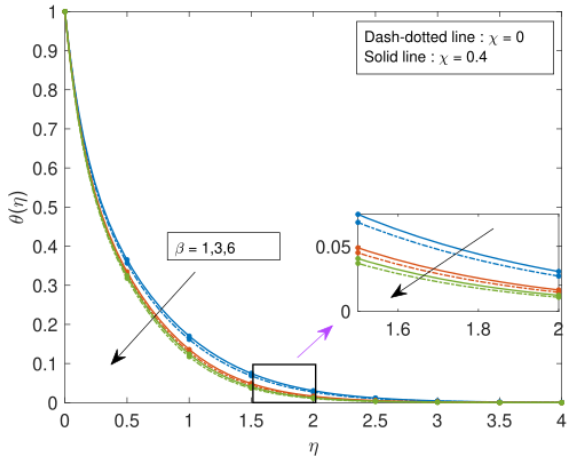

Fig. 13. Impact of the Williamson parameter, χ, and the Hall parameter, β, on $\theta(\eta)$

5.2 Combined Effect of the Williamson and the Porosity Parameter

Figure 14 to Figure 17 show the combined effect of the porosity and the Williamson parameter on the velocity profiles, $g'(\eta)$ and $h'(\eta)$, the concentration, $\theta(\eta)$, and the temperature distribution, $\omega(\eta)$. As the porosity parameter, γ, increases, $g'(\eta)$ consistently decreases. This suggests that the presence of the porosity parameter, which represents the ratio of the void volume to the total volume of a porous medium, reduces the velocity component in the x −direction. This is because the presence of solid obstacles or barriers can obstruct the flow of fluid, leading to reduced velocity. For $\chi = 0$, the $g'(\eta)$ profile remains consistently above that of $\chi = 0.4$, indicating that the shear-thinning properties introduced by the Williamson parameter, χ, have a diminishing effect on the velocity profile. The $h'(\eta)$ profile exhibits a more complex behaviour with an initial decrease and subsequent increase as γ increases. The high porosity parameters and fluid flow exhibit channelling or bypassing behaviour, where the fluid preferentially flows through certain pathways, hence increasing the flow in the vertical component. For $\chi = 0$, the $h'(\eta)$ profile is below that of $\chi = 0.4$, indicating that the shear-thinning property enhances the velocity of the flow in the y −direction. The concentration, $\theta(\eta)$, and the temperature distribution, $\omega(\eta)$, increase with a rise in the porosity parameter, γ. Increasing porosity typically leads to greater connectivity and openness of the porous medium, allowing for more efficient transport of heat and fluid bulk. As a result, temperature and

concentration gradients are reduced, and the overall temperature and concentration levels increase. For $\chi = 0$, the temperature and the concentration profiles are consistently below that of $\chi = 0.4$, indicating that the presence of the Williamson parameter contributes to a higher temperature and concentration. The shear-thinning properties of the Williamson parameter, χ, consistently impact the velocity profiles.

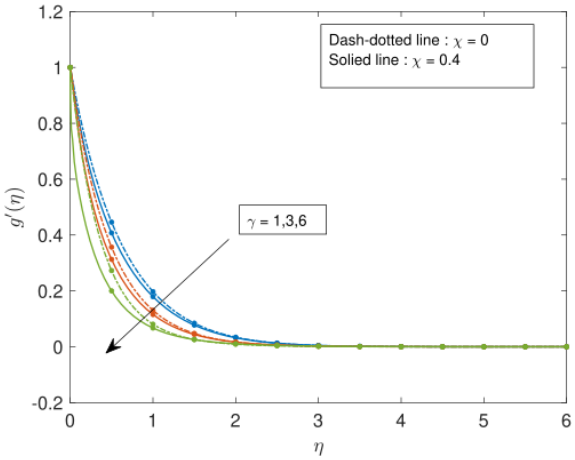

Fig. 14. Impact of the Williamson parameter, χ, and the porosity parameter, γ, on $g'(\eta)$

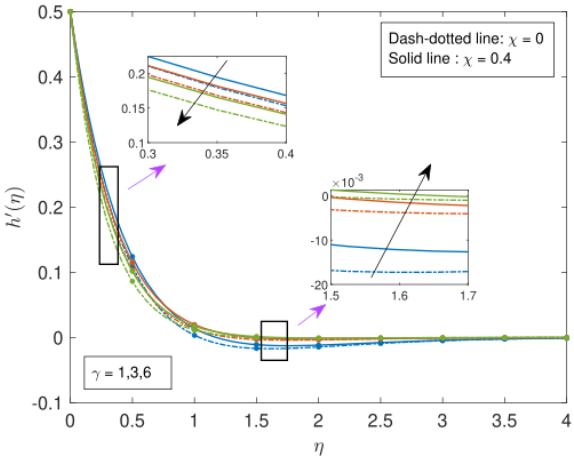

Fig. 15. Impact of the Williamson parameter, χ, and the porosity parameter, γ, on $h'(\eta)$

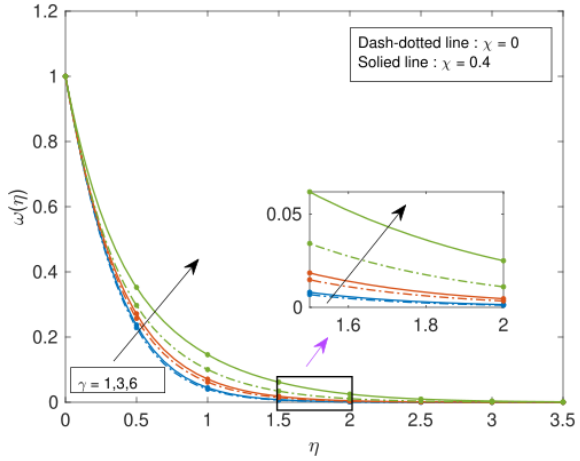

Fig. 16. Impact of the Williamson parameter, χ, and the porosity parameter, γ, on $\omega(\eta)$

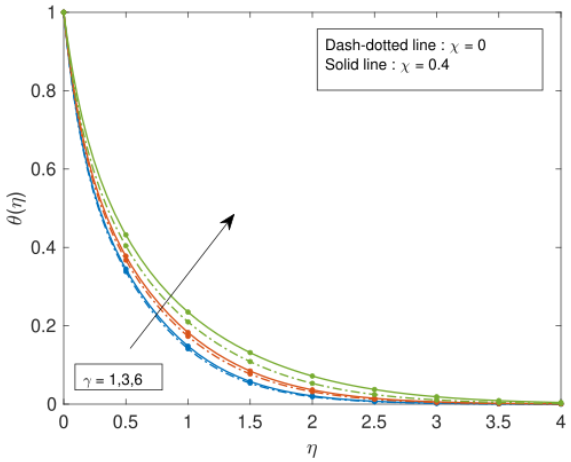

Fig. 17. Impact of the Williamson parameter, χ, and the porosity parameter, γ, on $\theta(\eta)$

5.3 Combined Effects of the Williamson and Chemical Reaction Parameters

Figure 18 to Figure 21 show the combined effects on $g'(\eta), h'(\eta), \theta(\eta)$, and $\omega(\eta)$, induced by the Williamson parameter and the chemical reaction parameter. The velocity profile, $g'(\eta)$, consistently decreases as the chemical reaction parameter K increases, indicating that higher values of K result in a reduction of the velocity component in the x −direction. Factors such as local fluid velocity, temperature, and concentration gradients can influence the rate of chemical reactions. In some cases, an increase in the chemical reaction parameter may lead to a decrease in fluid velocity due to the increased consumption of reactants or generation of products, which can alter the local flow field. For $\chi = 0$, the velocity profiles are consistently above those for $\chi = 0.4$. This suggests that the presence of the Williamson parameter contributes to a diminishing effect on the velocity profiles, especially with an increasing K. The velocity profile, $h'(\eta)$, increases as the chemical reaction

parameter, K, increases. This implies that higher values of K lead to an enhancement of the speed along the $y-$axis. For $\chi = 0$, the velocity profiles are consistently below those for $\chi = 0.4$. The presence of the Williamson parameter, χ, induces a shear-thinning behaviour, resulting in an enhanced velocity along the $y-$axis, especially with higher values of K. The temperature distribution, denoted as $\omega(\eta)$, exhibits an increase when the chemical reaction parameter, K, increases, demonstrating that larger values of K correspond to elevated temperatures. When comparing the cases where the Williamson parameter (χ) is equal to 0 and 0.4, it is clear that the temperature profiles are consistently higher for $\chi = 0.4$, indicating the significant influence of the Williamson parameter on temperature increase. Moreover, the concentration, denoted as $\theta(\eta)$, diminishes as K increases, indicating that larger values of K result in a drop in concentration. When comparing the cases where $\chi = 0$ and $\chi = 0.4$, it is observed that the concentration profiles for $\chi = 0$ consistently exhibit lower values. This indicates that the presence of the Williamson parameter, which is related to shear-thinning behaviour, leads to the reduction in concentration levels.

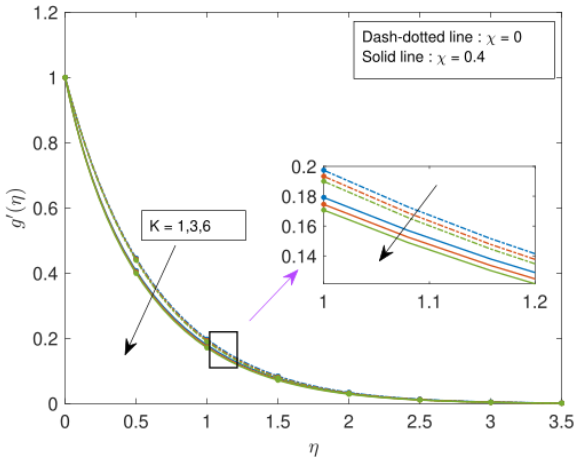

Fig. 18. Impact of the Williamson parameter, χ, and the chemical reaction parameter, K, on $g'(\eta)$

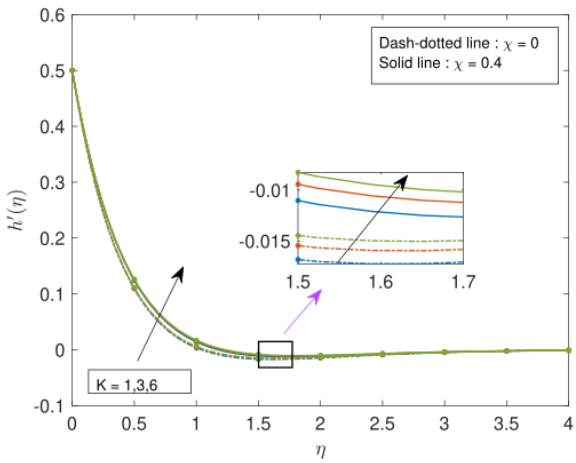

Fig. 19. Impact of the Williamson parameter, χ, and the chemical reaction parameter, K, on $h'(\eta)$

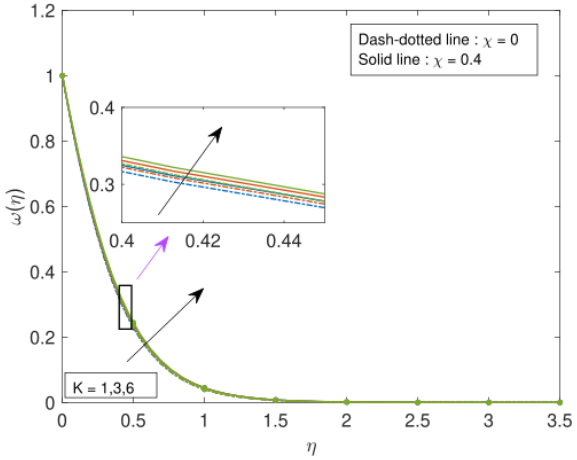

Fig. 20. Impact of the Williamson parameter, $\boldsymbol{\chi}$, and the chemical reaction parameter, $\boldsymbol{K}$, on $\boldsymbol{\omega(\eta)}$

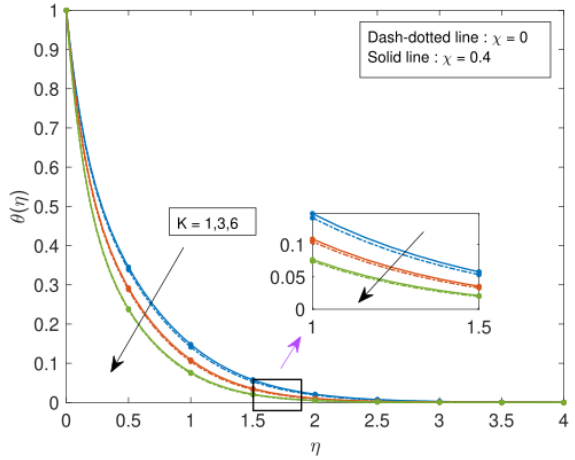

Fig. 21. Impact of the Williamson parameter, χ, and the chemical reaction parameter, K, on $\theta(\eta)$

5.4 Effect of the Magnetic Parameter

Figure 22 to Figure 25 display the impact of the magnetic parameter, M, on the velocity profiles, $g'(\eta)$ and $h'(\eta)$, temperature distribution, $\omega(\eta)$, and the concentration profile, $\theta(\eta)$. A higher value of the magnetic parameter leads to a reduction in the velocity profiles, $g'(\eta)$ and $h'(\eta)$. The decrease in the velocity profiles implies that stronger magnetic forces limit the movement of the fluid. The increased magnetic parameter can result in stronger forces that limit the velocity of fluid particles in both the x and y −directions. The increase of the magnetic parameter results in simultaneous rises in both the concentration, $\theta(\eta)$ and the temperature distribution, $\omega(\eta)$. The increased magnetic force results in the generation of heat, which in turn raises the temperature. Additionally, a strong magnetic force heightens the concentration of nanoparticles.

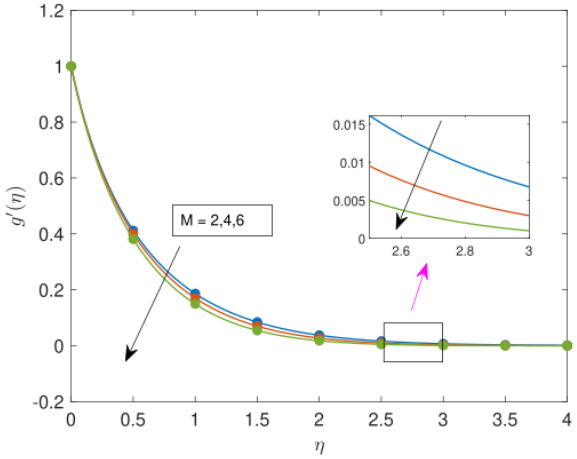

Fig. 22. The influence of the magnetic parameter, M, on $g'(\eta)$

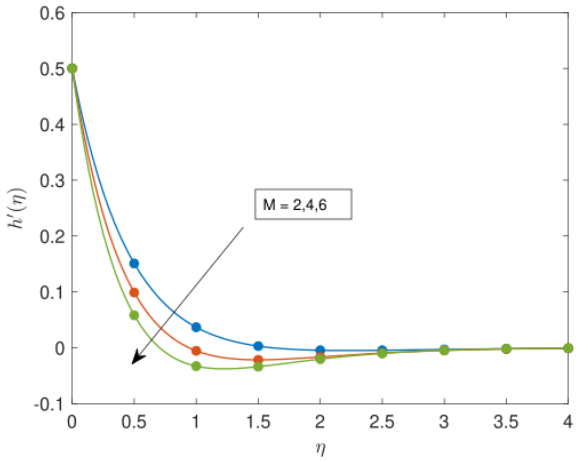

Fig. 23. The influence of the magnetic parameter, M, on $h'(\eta)$

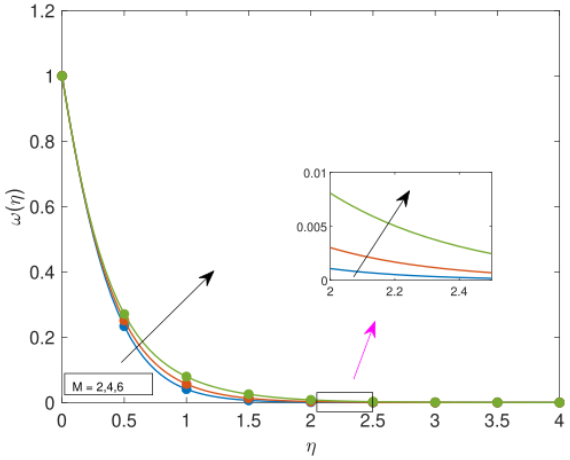

Fig. 24. The influence of the magnetic parameter, $\boldsymbol{M}$, on $\boldsymbol{\omega(\eta)}$

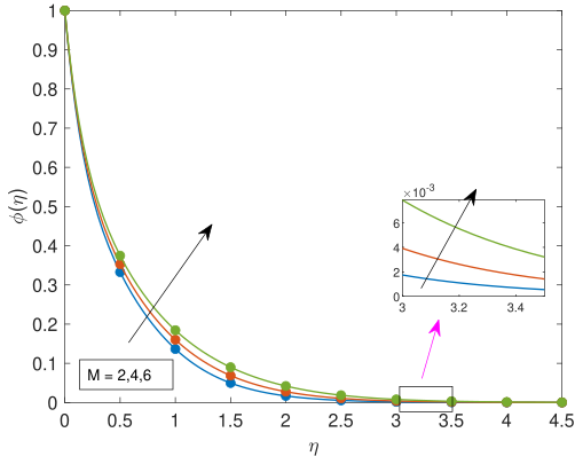

Fig. 25. The influence of the magnetic parameter, M, on $\theta(\eta)$

6. Conclusion

This study analyzed the magnetohydrodynamic (MHD) Williamson-nanofluid flow over an exponentially stretched surface. Using similarity transformations, the governing equations were converted into highly nonlinear ordinary differential equations (ODEs), which were then solved using

the overlapping multi-domain paired quasilinearization method (OMD-PQLM). Among the method's various solution options, the most efficient combination was selected to produce results.

The findings demonstrate the method's effectiveness in resolving the complex MHD Williamson-nanofluid model. The impacts of key parameters such as the Hall and chemical reaction parameters were evaluated, revealing that the Williamson parameter significantly influences the system behaviour, particularly in shaping velocity profiles, temperature distribution, and concentration. The shear-thinning properties of the Williamson fluid reduce the x −direction velocity component while increasing the y −direction component, resulting in higher temperature and concentration distributions. This study highlights the essential role of the Williamson fluid's shear-thinning effects on fluid dynamics, thermal properties, and mass transfer within the system.

It is important to note that a limitation of this study stems from the simplified assumptions that would affect the accuracy of results obtained, as well as the physical applicability of the results. Also, the range of parameters chosen was carefully selected to fall within the limit of the software used and the capacity of the machine. MATLAB 2023b was the software used in conducting the analysis.

The current study was based on a Williamson nanofluid flow over an exponentially stretched surface and the influence of some parameters on the flow. Further investigative studies are needed to perform comparative analysis for regular, hybrid, tri-hybrid and tetra-hybrid nanofluid for different flow geometries and study the effect of various factors on the flow of the fluid.

Acknowledgement
The authors express their gratitude to the anonymous reviewers for their valuable comments, which significantly enhanced the quality of this work.

References

[1] Williamson, R. Vo. "The flow of pseudoplastic materials." *Industrial & Engineering Chemistry* 21, no. 11 (1929): 1108-1111. https://doi.org/10.1021/ie50239a035

[2] Rana, B. M. J., S. M. Arifuzzaman, Saiful Islam, Sk Reza-E-Rabbi, Abdullah Al-Mamun, Malati Mazumder, Kanak Chandra Roy, and Md Shakhaoath Khan. "Swimming of microbes in blood flow of nano-bioconvective Williamson fluid." *Thermal Science and Engineering Progress* 25 (2021): 101018. https://doi.org/10.1016/j.tsep.2021.101018

[3] Khan, Umair, A. Zaib, A. Ishak, I. Waini, Zehba Raizah, and Ahmed M. Galal. "Features of magnetic field on biological Williamson fluid in radiated blood flow induced by gold particles through a curved moving surface with buoyancy effect." *International Journal of Modern Physics B* 37, no. 03 (2023): 2350021. https://doi.org/10.1142/S0217979223500212

[4] Haider, Irfan, Umar Nazir, M. Nawaz, Sayer Obaid Alharbi, and Ilyas Khan. "Numerical thermal study on performance of hybrid nano-Williamson fluid with memory effects using novel heat flux model." *Case Studies in Thermal Engineering* 26 (2021): 101070. https://doi.org/10.1016/j.csite.2021.101070

[5] Ali, Rashid, M. Riaz Khan, Awatef Abidi, Saim Rasheed, and Ahmed M. Galal. "Application of PEST and PEHF in magneto-Williamson nanofluid depending on the suction/injection." *Case Studies in Thermal Engineering* 27 (2021): 101329. https://doi.org/10.1016/j.csite.2021.101329

[6] Hadimani, Balachandra, Rajashekhar Choudhari, Prathiksha Sanil, Hanumesh Vaidya, Manjunatha Gudekote, Kerehalli Vinayaka Prasad, and Jyoti Shetty. "The influence of variable fluid properties on peristaltic transport of Eyring Powell fluid flowing through an inclined uniform channel." *Journal of Advanced Research in Fluid Mechanics and Thermal Sciences* 102, no. 2 (2023): 166-185. https://doi.org/10.37934/arfmts.102.2.166185

[7] Zaperi, Nur Husna Amierah Mohd, and Nurul Aini Jaafar. "Solute Dispersion in Casson Blood Flow through an Artery with the Effect of Electric Field." *Journal of Research in Nanoscience and Nanotechnology* 9, no. 1 (2023): 13-34. https://doi.org/10.37934/jrnn.9.1.1334

[8] Nadeem, S., and Noreen Sher Akbar. "Numerical solutions of peristaltic flow of Williamson fluid with radially varying MHD in an endoscope." *International Journal for Numerical Methods in Fluids* 66, no. 2 (2011): 212-220. https://doi.org/10.1002/fld.2253

[9] Liao, Shijun. "On the homotopy analysis method for nonlinear problems." *Applied Mathematics and Computation* 147, no. 2 (2004): 499-513. https://doi.org/10.1016/S0096-3003(02)00790-7

[10] Nadeem, S., and S. T. Hussain. "Flow and heat transfer analysis of Williamson nanofluid." *Applied Nanoscience* 4 (2014): 1005-1012. https://doi.org/10.1007/s13204-013-0282-1
[11] Gorla, Rama Subba Reddy, and B. J. Gireesha. "Dual solutions for stagnation-point flow and convective heat transfer of a Williamson nanofluid past a stretching/shrinking sheet." *Heat and Mass Transfer* 52 (2016): 1153-1162. https://doi.org/10.1007/s00231-015-1627-y
[12] Fehlberg, Erwin. *Classical seventh-, sixth-, and fifth-order Runge-Kutta-Nyström formulas with stepsize control for general second-order differential equations*. No. NASA-TR-R-432. 1974.
[13] Choi, Stephen U. S. "Nanofluids: from vision to reality through research." *ASME Journal of Heat and Mass Transfer* 131, no. 3 (2009): 033106. https://doi.org/10.1115/1.3056479
[14] Mkhatshwa, M. P., S. S. Motsa, M. S. Ayano, and P. Sibanda. "MHD mixed convective nanofluid flow about a vertical slender cylinder using overlapping multi-domain spectral collocation approach." *Case Studies in Thermal Engineering* 18 (2020): 100598. https://doi.org/10.1016/j.csite.2020.100598
[15] Mkhatshwa, Musawenkhosi, Sandile Motsa, and Precious Sibanda. "Overlapping multi-domain spectral method for conjugate problems of conduction and MHD free convection flow of nanofluids over flat plates." *Mathematical and Computational Applications* 24, no. 3 (2019): 75. https://doi.org/10.3390/mca24030075
[16] Shehzad, S. A., A. Rauf, T. Hayat, M. A. Meraj, and A. Alsaedi. "MHD stagnation point flow of micro nanofluid towards a shrinking sheet with convective and zero mass flux conditions." *Bulletin of the Polish Academy of Sciences Technical Sciences* (2017): 155-162. https://doi.org/10.1515/bpasts-2017-0019
[17] Galal, Ahmed M., Qusain Haider, Mubashar Arshad, Ali Hassan, Fahad M. Alharbi, Mohammad Mahtab Alam, and Thabet Abdeljawad. "Intelligent neural computing to investigate the heat and mass transmission in nanofluidic system between two rotating permeable disks: Supervised learning mechanism." *Case Studies in Thermal Engineering* 59 (2024): 104531. https://doi.org/10.1016/j.csite.2024.104531
[18] Galal, Ahmed M., Fahad M. Alharbi, Mubashar Arshad, Mohammad Mahtab Alam, Thabet Abdeljawad, and Qasem M. Al-Mdallal. "Numerical investigation of heat and mass transfer in three-dimensional MHD nanoliquid flow with inclined magnetization." *Scientific Reports* 14, no. 1 (2024): 1207. https://doi.org/10.1038/s41598-024-51195-4
[19] Zar, Pooriya Majidi, Bahram Jalili, Payam Jalili, and Davood Domiri Ganji. "Thermal study of magnetohydrodynamic nanofluid flow and Brownian motion between parallel sheets." *International Journal of Thermofluids* 23 (2024): 100806. https://doi.org/10.1016/j.ijft.2024.100806
[20] Arshad, Mubashar, Hanen Karamti, Jan Awrejcewicz, Dariusz Grzelczyk, and Ahmed M. Galal. "Thermal transmission comparison of nanofluids over stretching surface under the influence of magnetic field." *Micromachines* 13, no. 8 (2022): 1296. https://doi.org/10.3390/mi13081296
[21] Arshad, Mubashar, Azad Hussain, Ali Hassan, Hanen Karamti, Piotr Wróblewski, Ilyas Khan, Mulugeta Andualem, and Ahmed M. Galal. "Scrutinization of slip due to lateral velocity on the dynamics of engine oil conveying cupric and alumina nanoparticles subject to Coriolis force." *Mathematical Problems in Engineering* 2022, no. 1 (2022): 2526951. https://doi.org/10.1155/2022/2526951
[22] Zar, Pooriya Majidi, Payam Jalili, Bahram Jalili, and Davood Domiri Ganji. "Heat and mass transfer conduct in an unsteady two-dimensional stream between parallel sheets." *South African Journal of Chemical Engineering* 50 (2024): 109-124. https://doi.org/10.1016/j.sajce.2024.07.011
[23] Jalili, Payam, Zohreh Asadi, Amirali Shateri, Bahram Jalili, Hijaz Ahmad, M. Daher Albalwi, and Davood Domiri Ganji. "Thermal analysis of nanofluid magnetic flow on a rotating disk in the presence of radiation considering response surface method." *Modern Physics Letters B* 38, no. 24 (2024): 2450217. https://doi.org/10.1142/S0217984924502178
[24] Arshad, Mubashar, Fahad M. Alharbi, Abdullah Alhushaybari, Sayed M. Eldin, Zubair Ahmad, and Ahmed M. Galal. "Exploration of heat and mass transfer subjected to first order chemical reaction and thermal radiation: Comparative dynamics of nano, hybrid and tri-hybrid particles over dual stretching surface." *International Communications in Heat and Mass Transfer* 146 (2023): 106916. https://doi.org/10.1016/j.icheatmasstransfer.2023.106916
[25] Srinivasacharya, D., and Mekonnen Shiferaw. "Magnetohydrodynamic flow of a micropolar fluid in a circular pipe with hall effects." *The ANZIAM Journal* 51, no. 2 (2009): 277-285. https://doi.org/10.1017/S1446181110000039
[26] Ahmed, Sameh Elsayed, M. A. Mansour, Ahmed M. Rashad, and Z. Morsy. "MHD free convection and sinusoidal heating in a wavy cavity filled with a heat-generating porous medium using cu-water nanofluids." *Computational Thermal Sciences: An International Journal* 12, no. 3 (2020). https://doi.org/10.1615/ComputThermalScien.2020030316
[27] Nawaz, M., Shafia Rana, Imran Haider Qureshi, and T. Hayat. "Three-dimensional heat transfer in the mixture of nanoparticles and micropolar MHD plasma with Hall and ion slip effects." *AIP Advances* 8, no. 10 (2018). https://doi.org/10.1063/1.5050670

[28] Thomas, James William. *Numerical partial differential equations: finite difference methods*. Vol. 22. Springer Science & Business Media, 2013.
[29] Felippa, Carlos A. "Introduction to finite element methods." *University of Colorado* 885 (2004).
[30] Eymard, Robert, Thierry Gallouët, and Raphaèle Herbin. "Finite volume methods." *Handbook of Numerical Analysis* 7 (2000): 713-1018. https://doi.org/10.1016/S1570-8659(00)07005-8
[31] Cartwright, Julyan H. E., and Oreste Piro. "The dynamics of Runge-Kutta methods." *International Journal of Bifurcation and Chaos* 2, no. 03 (1992): 427-449. https://doi.org/10.1142/S0218127492000641
[32] Butcher, John. "Runge-kutta methods." *Scholarpedia* 2, no. 9 (2007): 3147. https://doi.org/10.4249/scholarpedia.3147
[33] Özişik, M. Necati, Helcio RB Orlande, Marcelo J. Colaço, and Renato M. Cotta. *Finite difference methods in heat transfer*. CRC Press, 2017. https://doi.org/10.1201/9781315168784
[34] Shashkov, Mikhail. *Conservative finite-difference methods on general grids*. CRC Press, 2018. https://doi.org/10.1201/9781315140209
[35] Motsa, Sandile S., and Isaac L. Animasaun. "Paired quasi-linearization analysis of heat transfer in unsteady mixed convection nanofluid containing both nanoparticles and gyrotactic microorganisms due to impulsive motion." *Journal of Heat Transfer* 138, no. 11 (2016): 114503. https://doi.org/10.1115/1.4034039
[36] Otegbeye, O., and S. S. Motsa. "A paired quasilinearization method for solving boundary layer flow problems." In *AIP Conference Proceedings*, vol. 1975, no. 1. AIP Publishing, 2018. https://doi.org/10.1063/1.5042190
[37] Samuel, Mutua. "Computational and numerical analysis of differential equations using spectral based collocation method." *PhD diss., University of Kwazulu-Natal*, 2019.
[38] Trefethen, Lloyd N. *Spectral methods in MATLAB*. Society for Industrial and Applied Mathematics, 2000. https://doi.org/10.1137/1.9780898719598